Eur. Phys. J. E (2005)
DOI 10.1140/epje/i2004-10087-y

THE EUROPEAN PHYSICAL JOURNAL E

Statistical mechanics of columnar DNA assemblies

A. Wynveen[a], D.J. Lee, and A.A. Kornyshev

Department of Chemistry, Imperial College London, SW7 2AZ London, UK

Received 1 August 2004 /
Published online: 7 February 2005 –

Abstract. Many physical systems can be mapped onto solved or "solvable" models of magnetism. In this work, we have mapped the statistical mechanics of columnar phases of ideally helical rigid DNA —subject to the earlier found unusual, frustrated pair potential (A.A. Kornyshev, S. Leikin, J. Chem. Phys. **107**, 3656 (1997))— onto an exotic, unknown variant of the XY model on a fixed or restructurable lattice. Here, the role of the "spin" is played by the azimuthal orientation of the molecules. We have solved this model using a Hartree-Fock approximation, ground-state calculations, and finite-temperature Monte Carlo simulations. We have found peculiar spin order transitions, which may also be accompanied by positional restructuring, from hexagonal to rhombohedric lattices. Some of these have been experimentally observed in dense columnar aggregates. Note that DNA columnar phases are of great interest in biophysical research, not only because they are a useful *in vitro* tool for the study of DNA condensation, but also since these structures have been detected in living matter. Within the approximations made, our study provides insight into the statistical mechanics of these systems.

PACS. 75.10.Hk Classical spin models – 87.15.Nn Properties of solutions; aggregation and crystallization of macromolecules – 64.70.-p Specific phase transitions – 87.14.Gg DNA, RNA

1 Introduction

DNA molecules in aqueous solution can be condensed into a variety of phases. As the density of DNA is increased, transitions occur from an isotropic liquid-like phase to a liquid-crystal phase and finally to a crystalline structure [1]. Within these phases, there exist configurations with different symmetries and molecular arrangements. For example, X-ray diffraction patterns of fibers of different species of alkali metal salts of DNA reveal that the DNA is crystallized into several different lattice types [2]. Likewise, liquid-crystalline mesophases with different symmetries, including cholesteric, line hexatic, and/or hexagonal columnar phases, have been observed over a wide range of DNA concentrations [1,3–5]. These mesophases are relevant for several reasons —indeed they are seen in many systems, such as bacteria, viruses, and mitochondria [6]. Understanding the structure of DNA aggregates may also aid in understanding the physics of DNA packing into sperm and phage heads [7] and gene therapy vesicles [8–10]. Last but not least, studies of these structures may shed light on the laws of DNA-DNA interaction, important, *e.g.*, in the problem of recognition of homologous genes [11]. As already mentioned, the specific phase of a DNA assembly depends heavily on DNA concentration, but many other factors, such as monovalent salt concentration and the effects of polycationic condensing agents in the solution, will also greatly influence the phase structure for a given DNA density [7,10]. These many factors, along with the complex chemical structure of DNA, complicate theoretical studies of these phases and the transitions between them. In many studies (see, for example, Ref. [12]) DNA molecules are treated as uniformly charged cylinders since DNA is a polyelectrolyte that dissociates in solution. This approximation works well at large interaction distances where counterions may screen the specific charge pattern of the DNA surface. But at the smaller separations, where liquid-crystalline structures are observed, a theory of the electrostatic interactions must take into account the discrete helical structure of DNA. Recent theoretical studies [13–15] have demonstrated that a number of phenomena can be rationalized with the help of such a theory. Indeed, after dissociating in solution, DNA preserves its double helical structure, with negative charges residing on phosphate strands and specifically adsorbing counter-cations settling in the grooves between the phosphates. This results in a helical charge separation motif along the DNA surface which dictates new interaction laws at close range. Reference [13] obtained a solution for the pair potential between helical macromolecules in parallel alignment, having in particular revealed that the interaction depends on the relative azimuthal orientation of the molecules about their long axes (negative charges on one molecule would like to be closer to the positive

[a] e-mail: a.wynveen@imperial.ac.uk

charges on the other). Recent work has shown that this azimuthal dependence yields a rich phase structure for columnar aggregates and may explain distortions in the hexagonal columnar phase [16,17], as well as a cholesteric to hexatic transition [18]. The findings of reference [13] allows a mapping of the pair interaction of DNA onto an XY-spin model of magnetism, albeit with an unusual spin coupling. In this report, we consider the effects of temperature on the structure of columnar phases in order to generate their full statistical mechanical description. Previous work [16] obtained ground-state configurations for the columnar phases, but incorporating temperature effects can change the properties of the transitions between these phases. Furthermore, they may give rise to more phases associated with the relative azimuthal orientation of the DNA molecules. We first develop a theory of columnar assemblies fixed on a hexagonal lattice. We find additional Berezinskii-Kosterlitz-Thouless–like and topologically related transitions in the "spin" structures when including temperature. Also, for a more complete picture of the columnar assemblies, we treat positional restructuring of the molecules at finite temperatures. Incorporating spatial degrees of freedom into a Monte Carlo simulation has yielded new insight into anomalous spatial correlations in columnar phases, which may also have relevance for transitions from columnar to cholesteric phases. These studies reveal lattice types similar to those obtained for the ground state [16] but great care must be taken due to the limitations of the interaction potential for certain situations. For example, at extremely large densities where the DNA is closely packed, water, specifically its temperature-dependent dielectric constant, can no longer be treated using its bulk properties as had been done to derive the interaction potential. Nevertheless, these results can be considered valid over a wide range of physical parameters and act as a first step to a completely atomistic approach which may explore a broader range of the physically relevant parameter space.

2 Hexagonal columnar assemblies

The calculation of the pair interaction between two DNA in parallel juxtaposition [13] regarded DNA as consisting of a double helical charge pattern of negative charges along the phosphate spine of the DNA and positive charges adsorbed into the grooves or on the phosphate strands (see Fig. 1). For identical rigid helices, the ground-state electrostatic interaction energy between two DNA duplexes of length L is given by

$$E_{\rm int} = L\left[a_0 - a_1\cos\left(\phi_1-\phi_2\right) + a_2\cos\left(2\left(\phi_1-\phi_2\right)\right)\right], \tag{1}$$

where the a coefficients depend on a variety of factors such as the charge distribution on the DNA and the dielectric properties of the solution, and they decay exponentially with interaxial spacing between the DNA [13,19]; for the most updated version of these expressions, see Appendix A of reference [20]. ϕ_i characterizes the azimuthal orientation of the middle of the minor groove of the i-th molecule relative to the direction of interaxial separation (Fig. 1).

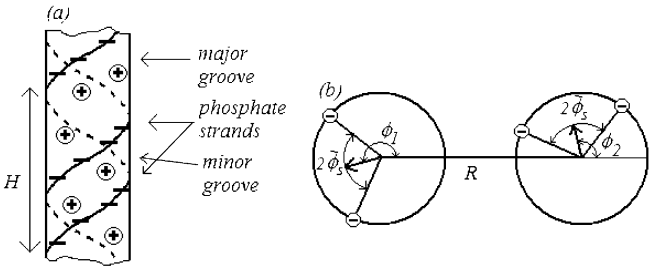

Fig. 1. The charge distribution of a single double helix (a) and the horizontal cross-section of two identical double helices in parallel juxtaposition (b), separated by interaxial spacing R. The DNA double helix shown is considered to consist of two spiralling negative phosphate strands with specifically adsorbing cations in its minor and major grooves. The pitch H of the helix for B-DNA is approximately 34 Å. In (b), $\tilde{\phi}_s$ (which is about 0.4π for B-DNA) is the angular half-width of the minor groove between the phosphate strands. "Spins" characterize the azimuthal orientations of the molecules; $\phi = \phi_1 - \phi_2$ is the angle of the relative azimuthal orientation of the molecules.

At large interaxial separations, the a_1 term dominates the a_2 term so the ground-state energy is minimized when the two duplexes have the same azimuthal orientations, *i.e.*, their "spins" look in the same direction, $\phi = \phi_1 - \phi_2 = 0$. But at separations below the point where $a_1 = 4a_2$, the energy is minimized when $\phi \neq 0$ and is degenerate: $\phi = \pm\phi_*$, where $\phi_* = \arccos\left[a_1/4a_2\right]$. In a hexagonal lattice, this gives rise to frustration between the neighboring spins which results in different spin phases for the ground state, depending on the relative strength of the a coefficients.

Since these electrostatic coefficients decay rapidly for increased spin separations, we need only consider nearest-neighbor interactions. The spin-dependent term in the Hamiltonian for a hexagonal phase of rigid DNA fragments of length L is given by the 2D hexagonal lattice XY model where there is an additional frustration term

$$H = -\,{}^1\!/_2 L a_1 \sum_{\langle ij\rangle}\cos\left(\phi_i-\phi_j\right) + {}^1\!/_2 L a_2 \sum_{\langle ij\rangle}\cos\left(2\left(\phi_i-\phi_j\right)\right) \tag{2}$$

with the summation over only nearest neighbors. The spin configuration of the ground state for this Hamiltonian is ferromagnetic, *i.e.*, all the spins are aligned, if $a_1 > 4a_2$. In the reverse case, the spins in the ground state are aligned in a three-state Potts [21] type configuration where the differences between the angles about any triangular plaquette on the lattice possess values related by [22]

$$\phi_2 - \phi_1 = \phi_1 - \phi_3 = \phi_{\rm potts}, \tag{3}$$

where

$$\phi_{\rm potts} = \arccos\left[\frac{1}{4}\left(1+\sqrt{1+\frac{2a_1}{a_2}}\right)\right]. \tag{4}$$

Utilizing a self-consistent Hartree-Fock approximation (HFA) [23], the free energy for a given spin configuration can be obtained at finite temperatures. Derivations of these free energies are left to the appendices. For the ferromagnetic state, where all the spins are aligned, the free energy is given by

$$F_{\rm fer} = \frac{Nk_{\rm B}T}{2}\ln\left(\frac{J}{k_{\rm B}T}\right) + Nk_{\rm B}T\hat{C}_{\rm Hex} + 3NL\left[a_0 - a_1\exp\left(-\frac{k_{\rm B}T}{6J}\right) + a_2\exp\left(-\frac{2k_{\rm B}T}{3J}\right)\right], \quad (5)$$

where N is the total number of spins, $\hat{C}_{\rm Hex} = -1.265$ is a constant that depends on the geometry of the lattice, and J is an effective coupling that is a solution to the transcendental equation

$$J = La_1\exp\left(-\frac{k_{\rm B}T}{6J}\right) - 4La_2\exp\left(-\frac{2k_{\rm B}T}{3J}\right). \quad (6)$$

The free energy for the Potts state is more cumbersome and has the form

$$\begin{aligned} F_{\rm potts} = {} & \frac{Nk_{\rm B}T}{2}\ln\left(\frac{J_1}{k_{\rm B}T}\right) \\ & + \frac{Nk_{\rm B}T}{6}\tilde{\Omega}_{\rm potts}(\alpha) + Nk_{\rm B}T\hat{C}_{\rm Hex} \\ & + 2NL\left[a_0 - a_1\cos\left(\psi_{\rm potts}\right)\exp\left(-\frac{\eta_1(\alpha)k_{\rm B}T}{J_1}\right)\right. \\ & \left. + a_2\cos\left(2\psi_{\rm potts}\right)\exp\left(-\frac{4\eta_1(\alpha)k_{\rm B}T}{J_1}\right)\right] \\ & + NL\left[a_0 - a_1\cos\left(2\psi_{\rm potts}\right)\exp\left(-\frac{\eta_2(\alpha)k_{\rm B}T}{J_1}\right)\right. \\ & \left. + a_2\cos\left(4\psi_{\rm potts}\right)\exp\left(-\frac{4\eta_2(\alpha)k_{\rm B}T}{J_1}\right)\right], \end{aligned} \quad (7)$$

where $\tilde{\Omega}_{\rm potts}$, η_1, and η_2 are given in Appendix C and are functions of the ratio of the coupling terms, $\alpha = J_2/J_1$. This equation is closed by the additional transcendental equations

$$\begin{aligned} J_1 = {} & La_1\cos\left(\psi_{\rm potts}\right)\exp\left(-\frac{\eta_1(\alpha)k_{\rm B}T}{J_1}\right) \\ & - 4La_2\cos\left(2\psi_{\rm potts}\right)\exp\left(-\frac{4\eta_1(\alpha)k_{\rm B}T}{J_1}\right), \end{aligned} \quad (8a)$$

$$\begin{aligned} J_2 = {} & La_1\cos\left(2\psi_{\rm potts}\right)\exp\left(-\frac{\eta_2(\alpha)k_{\rm B}T}{J_1}\right) \\ & - 4La_2\cos\left(4\psi_{\rm potts}\right)\exp\left(-\frac{4\eta_2(\alpha)k_{\rm B}T}{J_1}\right), \end{aligned} \quad (8b)$$

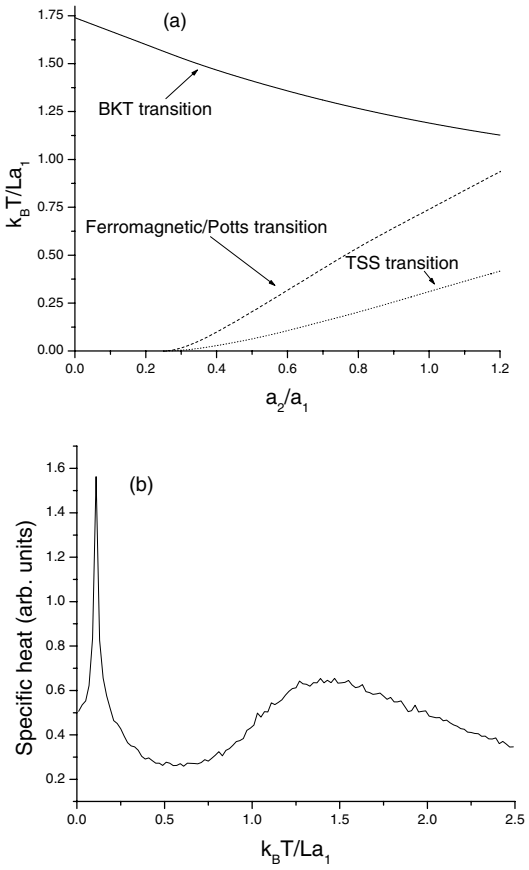

Fig. 2. Location (a) of the various transitions in a hexagonal lattice with nearest-neighbor interactions of equation (2). The TSS and BKT transitions are also observed as peaks in the specific heat (b), here shown for a coupling ratio $a_2/a_1 = 0.6$.

$$\begin{aligned} & a_1\sin\left(\psi_{\rm potts}\right)\exp\left(-\frac{\eta_1(\alpha)k_{\rm B}T}{J_1}\right) \\ & - 2a_2\sin\left(2\psi_{\rm potts}\right)\exp\left(-\frac{4\eta_1(\alpha)k_{\rm B}T}{J_1}\right) \\ & + a_1\sin\left(2\psi_{\rm potts}\right)\exp\left(-\frac{\eta_2(\alpha)k_{\rm B}T}{J_1}\right) \\ & - 2a_2\sin\left(4\psi_{\rm potts}\right)\exp\left(-\frac{4\eta_2(\alpha)k_{\rm B}T}{J_1}\right) = 0. \end{aligned} \quad (8c)$$

To find the transition line between the ferromagnetic and Potts states, the free energies (Eqs. (5) and (7)) are equated after solving the corresponding transcendental equations.

To obtain a full phase diagram, we also undertook Monte Carlo studies of the interaction Hamiltonian, equation (2), on the hexagonal lattice. The MC simulations were carried out in the standard manner using the Metropolis algorithm. A lattice site was chosen at random and the spin at this site was given a new random orientation. The new interaction energy between this site and its neighbors was calculated. If the new interaction energy was less than that of the original state, the new spin orientation was accepted. Otherwise, the new spin orientation was accepted with a probability according to

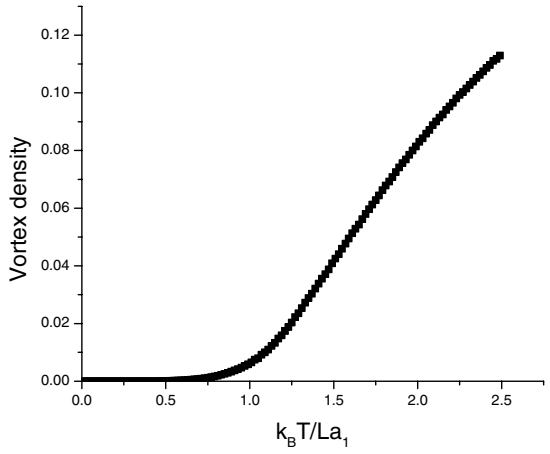

Fig. 3. The vortex density as a function of temperature for the same coupling ratio as in Figure 2(b). At the BKT transition, the vortex density begins to increase due to the unbinding of vortices in the lattice.

the Boltzmann factor $\exp(-\Delta E/k_{\rm B}T)$, where ΔE was the difference between the new and old interaction energies. After equilibration in the system was reached, successive MC steps were used to build up the canonical distribution of the spin configurations to obtain thermodynamic quantities such as specific heat, magnetic susceptibility, etc.

In Figure 2(a) we display the phase diagram of the system in terms of the relative strengths of the a coefficients and the temperature. Also shown on this phase diagram is the location of the transition between the Potts and ferromagnetic states obtained from the analytical expressions of the free energies. The specific heat for the ratio of the couplings $a_2/a_1 = 0.6$ is shown in Figure 2(b). The two peaks correspond to the transitions labeled as the "TSS transition" and the "BKT transition" (defined below) in the phase diagram.

The BKT transition corresponds to the standard Berezinskii-Kosterlitz-Thouless transition observed in many 2D spin systems [24]. At this transition, unbinding of the vortices leads to an abrupt increase of the vortex density, defined as $(1/N)\sum_i (v_i)^2$ where v_i is the vorticity at lattice site i, which in turn is defined as $(1/2\pi)\sum_{\Delta}(\phi_i - \phi_j)$, the sum of the spin differences about a triangular plaquette in the lattice. Figure 3 exhibits the increase in the vortex density at this transition.

The peak in Figure 2(b) found at lower temperatures stems from the fact that there exist two topologically distinct ground states [25] of the Potts configuration (see Fig. 4(a)) akin to that seen in purely antiferromagnetic spin systems [26]. In Figure 4(a) the number in the center of each triangular plaquette corresponds to the positive helicity of that triangle, defined as the sum of the clockwise positive change in the spin angles over 2π as the triangle is traversed in the clockwise direction (not to be confused with the vorticity where the angle difference may have positive and negative values). This transition is apparent in a plot of staggered, *i.e.*, taking into account only

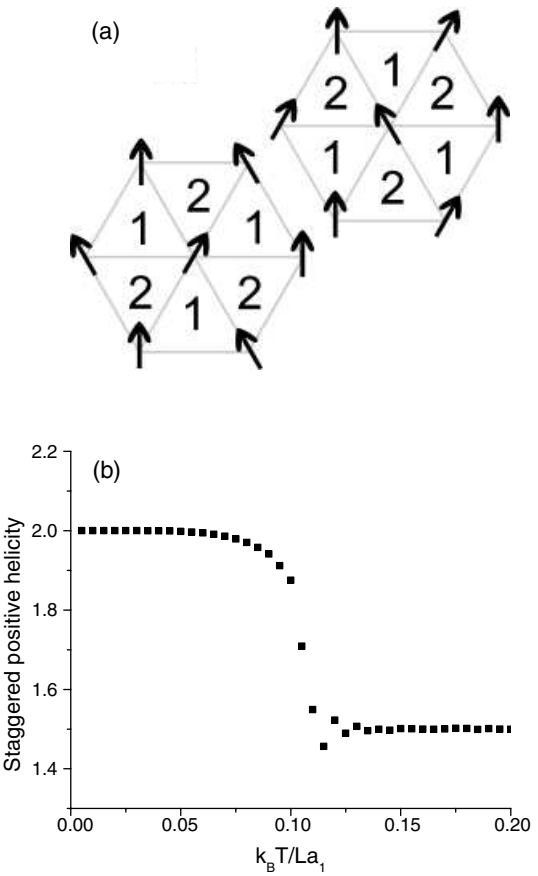

Fig. 4. Two topologically distinct ground states for the Potts configuration (a). At the TSS transition, domain walls between the two topologically distinct regions are excited so that each state becomes equally probable. This can be seen in a plot of the staggered positive helicity (defined in the text) as a function of temperature (b), shown again for the coupling ratio of Figure 2(b).

downward-pointing triangles in the lattice, positive helicity as the temperature changes (see Fig. 4(b)). Domain walls between these two distinct topologies are excited destroying the staggered helicity order at this transition, which we term the topological spin state (TSS) transition.

Comparisons can be made between the analytical forms, equations (5-8), and the MC simulations to confirm the validity of the two methods. Specific heats of the ferromagnetic and Potts states can be calculated from the free-energy expressions. For the ferromagnetic state in the region where $4a_2/a_1 < 1$, there is quite good agreement between the simulations and the analytic forms (Fig. 5(a)). As expected, deviations occur at higher temperatures where the HFA breaks down. Agreement between simulation and the analytical form for the Potts state, however, is not as good (Fig. 5(b)). Here, the specific heat obtained from the MC simulations diverges from the analytic form at relatively low temperatures. This discrepancy, as well as the fact that the Hartree approximation cannot account for the phase transition, can be taken as further indication of the TSS transition. The Hartree

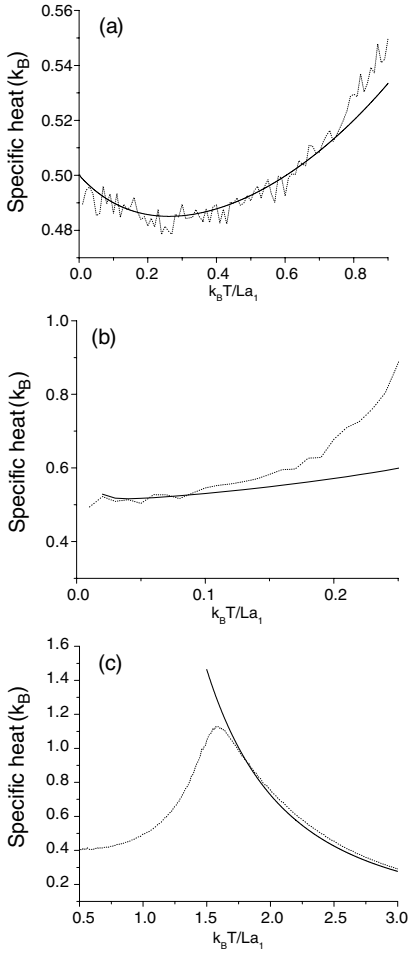

Fig. 5. Comparisons of the specific heat found from analytical forms (solid lines) to that obtained from the MC simulations (dotted lines). Results are displayed for the ferromagnetic state (a) for a coupling ratio $a_2/a_1 = 0.1$, the Potts state (b) for a coupling ratio $a_2/a_1 = 1.0$, and finally for the vortex regime (c) for a coupling ratio $a_2/a_1 = 0.2$.

approximation on its own neglects all topological excitations [27]. Therefore, this difference starts being significant at relatively low temperatures since domain walls may be excited quite easily. Also shown in Figure 5(c) is a high-temperature expansion of the specific heat for the Kosterlitz-Thouless vortex state given by

$$\frac{C_{\rm KT}}{k_{\rm B}} = \frac{3}{2}\left(\frac{(La_1)^2+(La_2)^2}{(k_{\rm B}T)^2}\right) + 3\left(\frac{(La_1)^3-(La_2)^3}{(k_{\rm B}T)^3}\right) - \frac{9}{16}\left(\frac{(La_1)^4+(La_2)^4}{(k_{\rm B}T)^4}\right), \quad (9)$$

which conforms quite well to the simulations.

Now that we have constructed the phase diagram for the 2D hexagonal lattice with spin interactions given by the Hamiltonian of equation (2) for generic values of the electrostatic a coefficients, we can use their calculated values from reference [20] to obtain results for "real" DNA columnar phases. Since these coefficients depend on the dielectric constant of the solution, which is temperature dependent, the coefficients too depend on temperature. Furthermore, interactions between DNA pairs are screened by charges in the solution, and so these coefficients are functions of the effective inverse Debye screening length. In a polyelectrolyte assembly with Donnan equilibrium [28], this is given by [16]

$$\kappa = \sqrt{4\pi \frac{(Z\rho/L + 2n_s)\, e^2}{\varepsilon k_{\rm B} T}} \quad (10)$$

and so there is an additional temperature dependence in the coefficients. Here, e is the electron charge, n_s is the salt concentration, ρ is the 2D DNA density in the columnar assembly, and $Z\,|e|$ is the uncompensated DNA charge (the fraction of the negative phosphate backbone that is not compensated by readsorbed cations). After finding the coefficients over a range of relevant temperatures and densities for a given charge distribution on the DNA and salt concentration, we simply map these coefficients onto the phase diagram of Figure 2(a) at the corresponding temperature to find where the transitions occur.

For ambient conditions at which columnar phases are observed *in vivo* or *in vitro*, the BKT transition would unlikely be observed. The relative strength of thermal energy to the interaction energy, which is on the order of unity at the BKT transition, would engender that extremely high, physically unviable, temperatures would be necessary to reach this transition. Rather, instead of going to high temperatures, the electrostatic interactions could be weakened, namely by increasing the salt concentration or increasing the interaxial distances between the DNA molecules, so that thermal energies would be comparable to the interaction energy. But at such low densities, the DNA would no longer be in a columnar aggregate. Likewise, at large salt concentrations (approximately ten times that of physiological levels) where this transition could be seen, the interaction between DNA would be so weak that we could not assume the DNA are pinned to the hexagonal lattice sites. In the next section, we will include the effects of thermally induced positional restructuring in the lattice showing that such effects certainly cannot be neglected.

On the other hand, the TSS transition may occur at temperatures, DNA densities, and salt concentrations where columnar structures are observed in experiments. At this transition, the electrostatic interaction energy dominates the thermal energy of the DNA so that the DNA is essentially immobile within the assembly. In Figure 6 we show the location of this transition for DNA with different charge compensation, *i.e.*, the fraction of the negative charge on the DNA phosphate backbone that is compensated by readsorbed cations, and also different salt concentration in the solution [14]. For all of these cases, we assumed that 30% of the cations readsorbed into the minor groove and 70% into the major groove of the DNA. To obtain this phase diagram, we took the length of the DNA molecules to be $L_p = 50\,$nm, which is the persistence length of DNA.

We must be careful, however, since this transition occurs at relatively small interaxial spacings where the

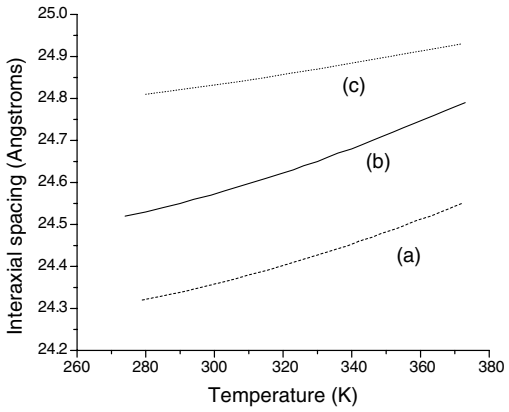

Fig. 6. Location of the TSS transition for different charge distributions on the DNA and different salt concentrations in the solution. The topologically disordered state lies above the curves, corresponding to lower densities. The dashed line (a) corresponds to a charge compensation of 0.9 with 0.1 M salt concentration. The solid line (b) and the dotted line (c) correspond to a charge compensation of 0.7 with 0.1 M salt solution for (b) and 1.0 M for (c). The effects are non-trivial, as they are driven mainly by the variation of κ (Eq. (10)) which changes the balance between the electrostatic coefficients a_1 and a_2.

continuum electrostatic theory, which underlies the Hamiltonian of equation (2), may break down. Although these spacings are quite small, they are close to the Debye screening length and so the linearized Poisson-Boltzmann equation used to derive the interaction [13] may still be valid at first approximation. However, dielectric response of water in the confined intracolumnar space may be different than in the bulk: most likely the effective dielectric constant of water will be reduced there. Its variation from the bulk value will vary with the density of the aggregate. This would slightly shift the transition to larger interaxial spacings, because of an increase in the electrostatic interactions between the DNA but would not eliminate this transition altogether.

3 Positional restructuring of the assembly

So far, we have assumed that the DNA molecules are pinned to sites on a hexagonal lattice. However, thermal motion, especially when the interactions become weak, may distort the lattice and, hence, affect the statistical mechanical properties of the system. Furthermore, depending on the form of the interaction, namely the interplay among the a coefficients, the hexagonal lattice may not be the optimal ground state of the system. Previous experimental and theoretical works have demonstrated that the 2D lattice of a columnar assembly may be distorted hexatic [4,17] or, almost equivalently, rhombic [16]. To incorporate these effects, we must modify our model for the columnar phases of the previous section.

To build up the statistical mechanical theory for columnar assemblies including positional restructuring, the ground-state configuration of the system is first obtained by performing a lattice sum of the interactions among the DNA molecules in the assembly [16]. Upon carrying out the lattice summation, we find that the ground-state configuration for certain values of the electrostatic coefficients is no longer hexagonal but rather rhombic as seen in reference [16]. For this structure, the spins possess a quasi-antiferromagnetic-Ising (QAF) ordering: spins at opposite diagonals of the rhombic cell are the same but there is a finite difference between the spins at adjacent corners (see Fig. 7). This is quite understandable qualitatively: parallel spins will repel each other due to the frustration-inducing a_2 interaction term thus distorting the hexagonal lattice. The degree of this distortion again rests on the interplay of the a terms in the interaction.

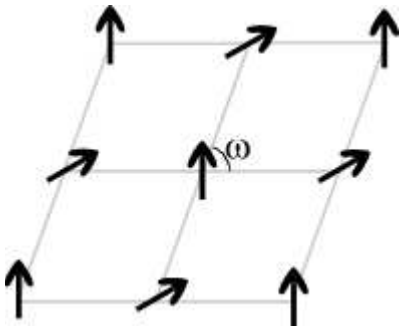

Fig. 7. The rhombic QAF state showing the distortion from the hexagonal lattice ($\omega \geq 60°$). Parallel spins lie at opposite corners of the rhombi, whereas spins with parameter-dependent differences lie at adjacent corners.

As before, we have derived an analytical expression for the free energy for this configuration taking into account only the six nearest neighbors. Here, however, due to the distortion, the electrostatic coefficients each take on two values according to the direction taken along the lattice: four of the nearest neighbors are at adjacent corners and the remaining two at the opposite corners along the short diagonal. Note, that this neglects neighbors across the long diagonal, but excluding these can be justified as long as the distortion angle is not much larger than 60°, which is generally the case. The free energy for this state is given by

$$
\begin{aligned}
F_{\rm af} &= \frac{Nk_{\rm B}T}{2}\ln\left(\frac{J_1}{k_{\rm B}T}\right) + \frac{Nk_{\rm B}T}{6}\tilde{\Omega}_{\rm af}\left(\alpha+\frac{1}{2}\right) + Nk_{\rm B}T\hat{C}_{\rm Hex} \\
&+2NL\left[a_0(R_1) - a_1(R_1)\cos\left(\psi_{\rm af}\right)\exp\left(-\frac{k_{\rm B}T}{\pi J_1}\arcsin\frac{1}{\sqrt{2\left(\alpha+1\right)}}\right)\right. \\
&\left. +a_2(R_1)\cos\left(2\psi_{\rm af}\right)\exp\left(-\frac{4k_{\rm B}T}{\pi J_1}\arcsin\frac{1}{\sqrt{2\left(\alpha+1\right)}}\right)\right] \\
&+NL\left[a_0(R_2) - a_1(R_2)\exp\left(-\frac{k_{\rm B}T}{2J_2}\left(1-\frac{4}{\pi}\arcsin\frac{1}{\sqrt{2\left(\alpha+1\right)}}\right)\right)\right. \\
&\left. +a_2(R_2)\exp\left(-\frac{2k_{\rm B}T}{J_2}\left(1-\frac{4}{\pi}\arcsin\frac{1}{\sqrt{2\left(\alpha+1\right)}}\right)\right)\right], \qquad (11)
\end{aligned}
$$

where $\alpha = J_2/J_1$, the form of $\tilde{\Omega}_{\rm af}$ is given in Appendix B, and the a coefficients are calculated at interaxial separations of R_1, the distance between differing spins, and $R_2 = R_1\sqrt{2-2\cos\omega}$, the distance between parallel spins across the short diagonal. The equation is closed by the

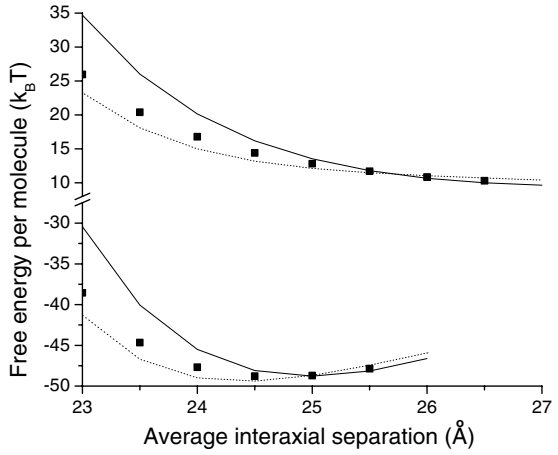

Fig. 8. The free energy for the QAF rhombic state (dotted line), Potts configuration (squares) and ferromagnetic hexagonal states (solid line) as a function of the average interaxial separation between nearest neighbors. The data are given for one persistence length long DNA and with charge distributions on the surface of 30% readsorbed cation charge in the minor groove and 70% in the major groove for a charge compensation of 0.9 (below the break in the y-axis) and of 0.7 (above the break). For a charge compensation of 0.9, the QAF rhombic state is the minimum energy configuration below a separation of about 25.0 Å (the Potts state is the lowest-energy configuration at smaller spacings (not shown)), and the ferromagnetic hexagonal state is the favorable configuration above this point. Likewise, for a DNA charge compensation of 0.7, this transition occurs at a separation of about 25.7 Å.

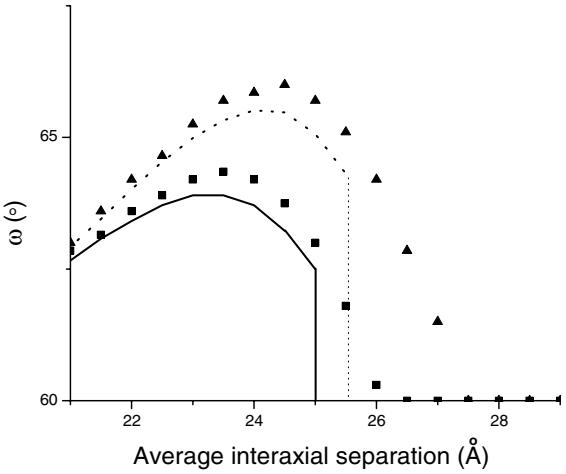

Fig. 9. Comparisons of the level of distortion (values of the rhombic angle ω) obtained from the analytic forms (lines) and the ground-state lattice summation (symbols) as a function of the average interaxial separation. Results are shown for a DNA charge compensation of 0.9 (solid line and squares) and of 0.7 (dotted line and triangles). The transition from the QAF rhombic state to the ferromagnetic state is of first order in the HFA calculation and occurs at smaller interaxial spacings as compared to the smooth crossover obtained from ground-state lattice sum calculations.

additional equations

$$J_1 = La_1(R_1)\cos(\psi_{\rm af})\exp\left(-\frac{k_{\rm B}T}{\pi J_1}\arcsin\frac{1}{\sqrt{2(\alpha+1)}}\right) - 4La_2(R_1)\cos(2\psi_{\rm af})\exp\left(-\frac{4k_{\rm B}T}{\pi J_1}\arcsin\frac{1}{\sqrt{2(\alpha+1)}}\right), \quad (12a)$$

$$J_2 = La_1(R_2)\exp\left(-\frac{k_{\rm B}T}{2J_2}\left(1-\frac{4}{\pi}\arcsin\frac{1}{\sqrt{2(\alpha+1)}}\right)\right) - 4La_2(R_2)\exp\left(-\frac{2k_{\rm B}T}{J_2}\left(1-\frac{4}{\pi}\arcsin\frac{1}{\sqrt{2(\alpha+1)}}\right)\right), \quad (12b)$$

$$\cos(\psi_{\rm af}) = \exp\left(-\frac{3k_{\rm B}T}{\pi J_1}\arcsin\frac{1}{\sqrt{2(\alpha+1)}}\right)\frac{a_1(R_1)}{4a_2(R_2)}. \quad (12c)$$

Solving equations (11) and (12), we can find the amount of distortion that minimizes the free energy. Figure 8 shows comparisons between the analytic forms for the free energy at a temperature of 300 K for the various lattice types for a couple of different charge distributions on the DNA surface. Incorporating temperature via the HFA calculation leads to an abrupt first-order transition between the QAF rhombic state and the ferromagnetic hexagonal state, found from comparing the results of equation (5) and equation (11). This may well be an artifact of the HFA calculation [20], but nevertheless, the transition becomes much sharper as compared to the smoother crossover found from the ground-state lattice sum calculation. This transition also occurs at a smaller interaxial spacing than where the ground-state lattice sum calculation yields the crossover between the two states. Including temperature also alters the amount of the distortion in the rhombic state, as shown in a plot of ω as a function of the average interaxial spacing in Figure 9, as compared to that found from the lattice sum calculations. At very large densities, the system returns once again to a hexagonal state with the Potts-type spin configuration. Also, as seen in Figure 8, the energy difference between the hexagonal Potts configuration and the QAF rhombic state is on the order of $k_{\rm B}T$, and so there may be a mixture of these phases at certain densities. Again, these results are subject to the limitations of the derived pair interaction at small interaxial spacings mentioned previously.

As before, we perform Monte Carlo simulations on the 2D columnar system. As opposed to the fixed lattice calculations of the previous section, here, however, a MC step either corresponds to a change in the spin or a change in position to probe both spin and spatial degrees of freedom. Again, the standard Metropolis algorithm is employed to build up the canonical distribution of the assembly at a specified temperature. The new energy is found by calculating the interactions of the molecule only with others that lie within a specified neighborhood of the original molecule. This is done to increase the efficiency of the simulation and is justified since the interactions decay quickly with increasing intermolecular distance. From the simulations, we obtain relevant thermodynamic quantities, upon

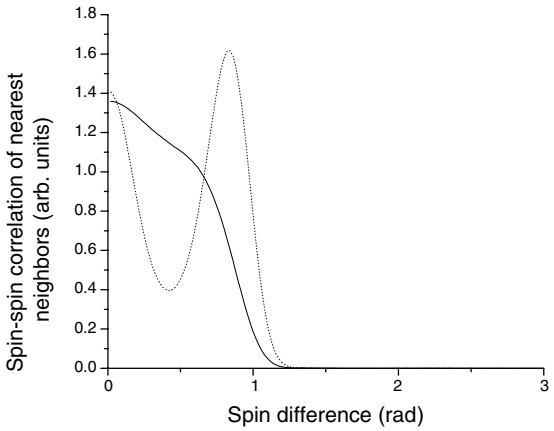

Fig. 10. The thermally averaged probability distribution of the spin difference between nearest neighbors near the transition between the QAF rhombic state and the ferromagnetic hexagonal state. The distributions are shown for a DNA charge compensation of 0.9 with the dotted line corresponding to an interaxial spacing of 24.5 Å and the solid line to the one of 25.4 Å at a temperature of 300 K.

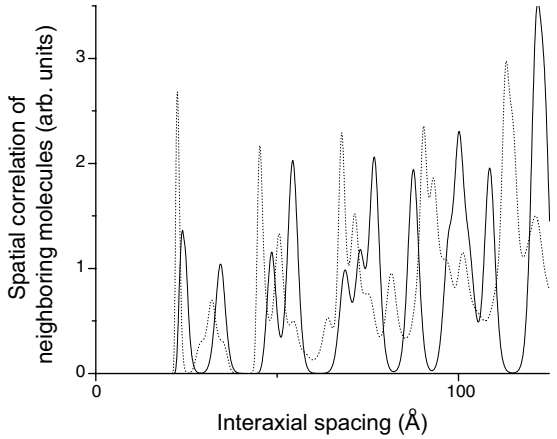

Fig. 11. The probability distribution of neighbors for a DNA surface charge distribution with 90% charge compensation where 50% of the cations are readsorbed in the minor groove and 50% in the major groove. The dotted line corresponds to an average interaxial nearest-neighbor spacing 24.2 Å and the solid line corresponds to an average spacing of 26.2 Å. As evident in the plot, the lower density distribution is more liquid-like where neighboring molecules have a finite probability to be at a broad range of interaxial spacings, whereas the lower density spatial distribution possesses a more crystalline ordering.

thermal equilibration of the system, as well as information concerning spin and positional correlations.

The QAF rhombic to ferromagnetic hexagonal transition shown in Figures 8 and 9 also appears in these simulations at the same average nearest-neighbor interaxial spacings found from our analytical explorations. In Figure 10, the distribution of the spin difference between nearest neighbors is shown for interaxial spacings just below and above this transition. As shown in this figure, the nearest-neighbor spin configuration develops from the two-state QAF phase to a broad single maximum about zero, the ferromagnetic phase. This is likewise observed in the spatial distribution between neighbors. Below the transition, the distribution shows nearest-neighbor, next-nearest-neighbor, etc. correlations that match a rhombic structure, while above the transition, the distribution matches that of a hexagonal lattice. Note that just beyond this transition at lower densities (at least for the charge distribution on the DNA used in the simulation that generated the results of Fig. 10), the DNA precipitates out of solution leaving a coexistence region of DNA aggregate and DNA-free solution [16].

In order to avoid the situation where DNA condenses out of solution at lower densities solely due to the choice of the charge distribution on the DNA, a charge distribution can be used where the interaction energy leads to a purely repulsive force between molecules. One such charge distribution is that where there the readsorbed cations are shared evenly between the major and minor grooves of the double helix. For this charge distribution, the interaction energy found by lattice sum calculations yields a flattening of the potential at intermediate densities that arises due to the spin frustration in the system. Due to this flattening, we find that as the density is increased, the spatial correlation function (the probability distribution of the location of neighboring molecules, $4\pi R^2 g(R)$) becomes more liquid-like. Results of the MC simulation are shown in Figure 11 demonstrating this effect. As the density is increased further, of course, the system once again becomes more crystalline. We essentially find here an effect which could be conventionally called spin-frustration–induced melting of the positional structure of the columnar aggregate.

In reference [18] analysis of the chiral electrostatic interaction for cholesteric liquid crystals demonstrated that biaxial correlations, *i.e.*, the ensemble-averaged azimuthal spin difference between nearest neighbors, determines the strength of the chiral interaction in the cholesteric phase. As these correlations grow larger, the chiral interaction, giving rise to the cholesteric phase, increases. These correlations, $\langle\cos(\phi)\rangle$ namely and $\langle\cos(2\phi)\rangle$, can easily be calculated from the thermally averaged distribution of the spin difference between nearest neighbors in our simulation. As shown in Figure 12, $\langle\cos(\phi)\rangle$ obtains its maximum value at an average interaxial separation of about 32 Å at the same point that $\langle\cos(2\phi)\rangle$ becomes positive. Interestingly, this spacing corresponds to that at which a transition between the columnar phase and the cholesteric phase is observed in experiments [29,30]. The transition between the QAF rhombic and ferromagnetic hexagonal phases, as shown in Figure 9 for different charge distributions, correspondingly occurs at this same spacing for this DNA charge distribution. As the interaxial spacing increases, these correlations decay to zero as a result of the overall weakening of the interactions between molecules at smaller densities, which leads to an isotropic liquid phase.

4 Discussion

We have presented results of a statistical mechanical analysis of DNA in columnar assemblies that interact via an

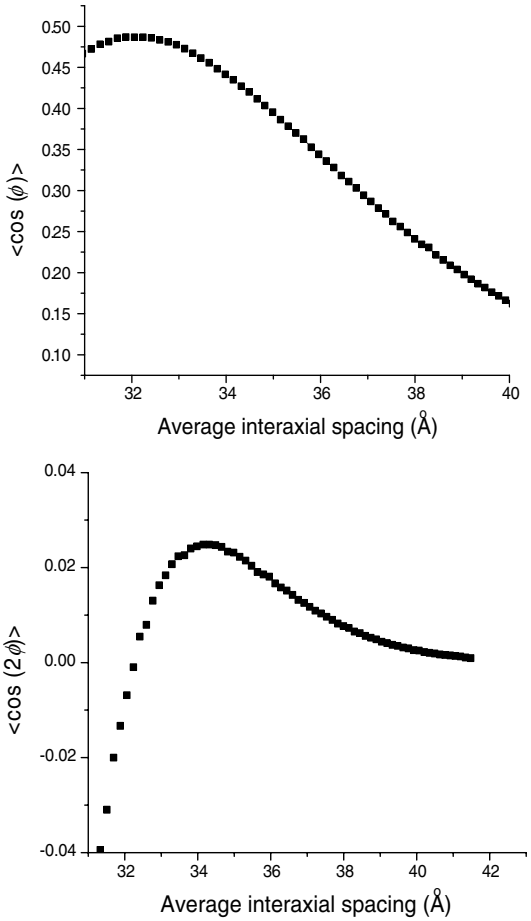

Fig. 12. Biaxial correlation functions calculated from the probability distribution of nearest-neighbor spin differences.

azimuthal angle ("spin") dependent pair potential [13]. Recent molecular-dynamics studies [31], in which no specific counterion readsorption on the DNA surface was assumed, demonstrate that the interaction loses this azimuthal dependence beyond surface-surface separations of only a few angstroms. Experimental evidence [32] reveals, however, that many of the counterions used to condense DNA preferentially absorb into the grooves of the DNA molecule and therefore would enhance the azimuthal dependence. Furthermore, a recent analysis [33] of X-ray diffraction patterns of columnar DNA assemblies at different densities shows the existence of azimuthal correlations, *i.e.* orientational ordering, of neighboring DNA molecules with interaxial separations of up to 40 Å or more. Thus, we believe that the form of potential we have used, which implies strong azimuthal correlations and in theory is responsible for the observed mesomorphism of DNA assemblies, has some experimental justification.

Initially, we assumed that DNA is packed in a fixed two-dimensional hexagonal structure so that we had to consider only "spin-spin" interactions between neighboring molecules. Hence, tools similar to those used for studying magnetic systems could be employed. Again, this spin interaction arises from the helical charge distribution on the double helix. Due to a quasi-antiferromagnetic coupling term in the interaction, the system may be frustrated, which gives rise to a rich phase structure.

Besides a Berezinskii-Kosterlitz-Thouless–type transition and an intermediate transition to a ferromagnetic-like state, we have found a transition associated with domain formation of two distinct topologies of the spin system. Comparing biologically relevant values of the spin coupling terms to the generic phase diagram of the hexagonal system, we find that this latter transition may be experimentally probed in dense assemblies. Calorimetric measurements would seem to be the simplest option to study this transition, but other experimental factors may inhibit a direct measurement of the transition in this manner. X-ray diffraction [4] or NMR [29] techniques, however, may be able to directly scrutinize the spin structure within the assembly to obtain the spin correlations in the system thus providing evidence if such a transition exists. Investigations are currently being pursued by our experimental collaborators at Imperial College London.

Extending the theory, we considered non-hexagonal lattice types and also incorporated thermally induced positional fluctuations of the molecules. Previous studies of DNA assemblies [16] demonstrated that a 2D rhombic (distorted hexagonal) lattice would be the ground-state configuration of the system under certain conditions. We found from both analytical and numerical investigations a first-order transition from this quasi-antiferromagnetic rhombic state to a hexagonal ferromagnetic state as the density of DNA in the system decreases. Likewise, this transition also appears in the probability distribution of the nearest-neighbor phase angle difference of the MC simulations. The ensemble average of nearest-neighbor spin differences develops from a two-state spin system to one with a single maximum.

Furthermore, these MC simulations revealed other interesting phenomena. For certain distributions of adsorbed cations on the DNA surface, we found that increasing the DNA density lead to a counterintuitive reduction in the crystalline ordering of the system so that the system became more liquid-like. This has been observed in classical experiments [4] of densely packed DNA at roughly the same interaxial spacings as those found in our simulations. Again, this results from the frustration in the spin interaction between the molecules. Also, in this same system, we found that the behavior of biaxial correlations between neighboring molecules, which has been proposed as a mechanism underlying the formation of cholesteric phases [18] at densities lower than those of the columnar phases, is influenced by the transition between the quasi-antiferromagnetic rhombic and ferromagnetic hexagonal phases. This occurs at interaxial spacings where the transition between columnar and cholesteric phases are observed in experiments. As the density of the DNA assembly is further decreased, the intermolecular interactions would grow ever weaker, until, finally, thermal motion would destroy any lattice ordering in the system. At this point, the lattice would then completely melt into a liquid-like isotropic phase [34].

Throughout this paper we have used a 2D model to describe interactions between DNA. In three dimensions, as well as azimuthal angular fluctuations, there exist fluctuations of the relative positions of the molecules along their long axes. If the charge distribution of the DNA surface is taken as continuous, then these two types of fluctuations are indistinguishable in the roles they play in the interaction energy, *i.e.*, an azimuthal rotation is equivalent to a translation along the long axis. For this case, we may simply replace the azimuthal coordinate ϕ by the coordinate $\tilde{\phi} = \phi - 2\pi z/H$ in all our expressions, which would not alter our present results. However, if we consider that the charges on the DNA surface are discrete, this equivalence will be lost; there will be additional interactions which destroy this symmetry. Nevertheless, if the assemblies are not extremely dense, these additional interactions due to discreteness can be neglected and the charge pattern on the DNA can be considered to be continuous. Still, discreteness will restrict the corkscrew motion ($\tilde{\phi} = 0$) of DNA, which costs no energy for a continuous charge distribution, within the assemblies.

We must caution once again that the form of the DNA-DNA interaction [13] we have employed is subject to certain limitations. As the concentration of DNA in the solution is increased, so that the surface-to-surface separation becomes prohibitively small, effects of non-local polarizability of the water in the narrow interstitial regions between the DNA could alter the results [35]. Furthermore, dielectric saturation and sterical constraints threaten to freeze the dielectric response of strongly confined water. Likewise, at such large densities, steric forces between DNA mediated by confined water may need to be also included in the interaction. Also, the pair potential was derived using a linearized Poisson-Boltzmann equation which is valid for weak electric fields in solution, and thus the pair potential may not be valid when the electrostatic interactions are quite substantial (large densities). Next, as the DNA concentration is altered or the DNA move about, rearrangement or additional adsorption/desorption of cations on the DNA surface may occur in response to a change in intermolecular distances [28], thus affecting the pair interaction. Last but not least, in this study DNA duplexes have been considered as ideally helical: sequence-dependent distortions from an ideal double helical step structure of DNA [19] have been neglected here as well as the torsional elasticity of the duplexes, that in columnar aggregates can correct the non-ideality [20,22,36]. Nevertheless, this is a first step to rationalize the columnar systems at finite temperatures before treating them with a computationally expensive fully atomistic approach in which these results may be tested.

This work has been strongly stimulated by the Monte Carlo simulations of DNA columnar assemblies of G. Sutmann and many detailed discussions of this subject with him and also with S. Leikin. Financial support from EPSRC grant No. GR/S31068/01 and a Royal Society Wolfson Merit Research award to A.A.K. are gratefully acknowledged.

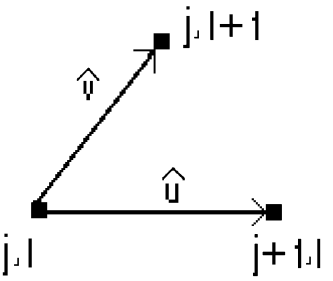

Fig. 13. Lattice labelling and relative positions of $\hat{u}$ and $\hat{v}$.

Appendix A. The Hartree approximation for the ferromagnetic state

The partition function for our modified XY model is

$$Z = \prod_{jl} \int \mathrm{d}\phi_{j,l} \exp\left(-\frac{E[\phi_{j,l}]}{k_{\mathrm{B}}T}\right), \tag{A.1}$$

where we may rewrite equation (2) of the text as

$$E[\phi_{j,l}] = L\sum_{p=1}^{2}\sum_{j,l} a_p(-1)^p[\cos(p(\phi_{j,l}-\phi_{j,l-1})) + \cos(p(\phi_{j,l}-\phi_{j-1,l}))+\cos(p(\phi_{j,l}-\phi_{j-1,l+1}))]. \tag{A.2}$$

Here, we have introduced two lattice vectors $\boldsymbol{u}_i = jr_0\hat{u}$ and $\boldsymbol{v}_j = lr_0\hat{v}$, where $\hat{u}$ and $\hat{v}$ are unit vectors, to describe the relative positions of the sites (DNA molecules) in the hexagonal lattice. The relative positions of these two vectors, as well as site labelling, are shown in Figure 13. We then start by expanding out $E[\phi_{j,l}]$ in powers of ϕ and dividing the energy into a Gaussian part as well as an anharmonic part, which contains terms of higher order than two in the expansion:

$$E[\phi_{j,l}] = E_0[\phi_{j,l}] + E_{\mathrm{anh}}[\phi_{j,l}],$$

$$E_0[\phi_{j,l}] = 3NL(a_2-a_1) + \frac{m_0}{2}\sum_{j,l}\left[(\phi_{j,l}-\phi_{j-1,l})^2 + (\phi_{j,l}-\phi_{j,l-1})^2+(\phi_{j,l}-\phi_{j-1,l+1})^2\right], \tag{A.3}$$

$$E_{\mathrm{anh}}[\phi_{j,l}] = \sum_{j,l}\sum_{n=2}^{\infty}\frac{1}{(2n)!}\left[\left(La_1(-1)^{n-1} + La_2(-4)^n\right) \times \left((\phi_{j,l}-\phi_{j-1,l})^{2n}+(\phi_{j,l}-\phi_{j,l-1})^{2n}+(\phi_{j,l}-\phi_{j-1,l+1})^{2n}\right)\right],$$

where N ($N \gg 1$) is the number of sites in our system, and $m_0 = L(a_1 - 4a_2)$. We introduce the following lattice Fourier transform:

$$\phi_{l,j} = \frac{1}{\sqrt{A}}\sum_{k_u,k_v}\phi(\boldsymbol{k})e^{i(jk_u+lk_v)r_0}, \tag{A.4}$$

where A is total area of the lattice and r_0 is the lattice spacing. We have chosen reciprocal-lattice vectors corresponding to the rhombic Bravais lattice defined by $\hat{u}$ and

$\hat{v}$. Then k_u and k_v take on values which lie within the first Brillouin zone for a rhombic lattice ($-\pi/r_0 < k_u < \pi/r_0$). This is not the only way we could choose our reciprocal lattice; another possible choice corresponds to the first Brillouin zone of the hexagonal lattice [37]. However, we have been able to show the equations we obtain do not depend on this choice, and it is far easier to use the rhombic Brillouin zone. Using equation (A4) we may rewrite our partition function as

$$Z = \int D\phi(\boldsymbol{k}) \exp\left(-\frac{E_0[\phi(\boldsymbol{k})] + E_{\rm anh}[\phi(\boldsymbol{k})]}{k_{\rm B}T}\right), \quad \text{(A.5)}$$

where

$$E_0 = \frac{Nm_0}{2V}\sum_k \phi(\boldsymbol{k})\,(2-2\cos(k_a r_0)) + (2-2\cos(k_b r_0)) + (2-2\cos((k_a-k_b)r_0)))\,\phi(-\boldsymbol{k}) \quad \text{(A.6)}$$

and

$$E_{\rm anh}[\phi(\boldsymbol{k})] = L\sum_{n=2}^{\infty}\frac{a_1(-1)^{n-1}+a_2(-4)^n}{(2n)!}\frac{N}{V^n}\delta_{-k_1,k_n+k_{n-1}+\ldots k_2} \times\left[\prod_{m=1}^{2n}\sum_{k_m}\phi(\boldsymbol{k}_m)\left(1-e^{-ik_{mu}r_0}\right) + \prod_{m=1}^{2n}\sum_{k_m}\phi(\boldsymbol{k}_m)\left(1-e^{-ik_{mv}r_0}\right) + \prod_{m=1}^{2n}\sum_{k_m}\phi(\boldsymbol{k}_m)\left(1-e^{-i(k_{mu}-k_{mv})r_0}\right)\right], \quad \text{(A.7)}$$

where $\boldsymbol{k}_m = (k_{mu}, k_{mv})$, thus diagonalizing the "free" part of the energy.

Let us consider the free energy for Gaussian fluctuations, where we neglect $E_{\rm anh}$. Here, we may integrate over $\phi(\boldsymbol{k})$ and so obtain the free energy for $N \gg 1$:

$$F_0 = 3NL(a_1-a_2) + \frac{k_{\rm B}TNL}{2(2\pi)^2}\int_{-\pi}^{\pi}{\rm d}x\int_{-\pi}^{\pi}{\rm d}y\;\ln\Big(\frac{m_0}{\pi}\left[(2-\cos x) + (2-\cos y) + (2-2\cos(x-y))\right]\Big). \quad \text{(A.8)}$$

The exact numerical calculation of the integral gives us

$$F_0 = 3NL(a_1-a_2) + \frac{k_{\rm B}TNL}{2}\ln m_0 + 0.235 k_{\rm B}TNL. \quad \text{(A.9)}$$

For the Gaussian correlation function,

$$G_0(\boldsymbol{k}) = Z^{-1}\int D\phi(\boldsymbol{k})\phi(\boldsymbol{k})\phi(-\boldsymbol{k})\exp\left(-\frac{E_0[\phi(\boldsymbol{k})]+E_{\rm anh}[\phi(\boldsymbol{k})]}{k_{\rm B}T}\right), \quad \text{(A.10)}$$

it is easy to show that

$$G_0(\boldsymbol{k}) = k_{\rm B}T\left[m_0\left((2-2\cos(k_u r_0)) + (2-2\cos(k_v r_0)) + (2-2\cos((k_u-k_v)r_0))\right)\right]^{-1}. \quad \text{(A.11)}$$

To obtain the Hartree approximation we must develop the perturbation theory for the full correlation function. We will omit details on how one obtains the expansion [38],

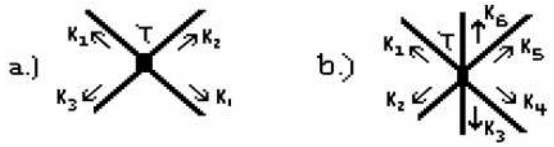

Fig. 14. a) represents all three types of vertices for the φ^4 term in the expansion for $E_{\rm anh}$. Shown, here, are the four wave vectors associated with each φ^4 vertex. Also, we write an index $\tau = 1, 2, 3$ which distinguishes between these three types. In the corresponding expression there is a particular form factor associated with each of the three types of vertex we may draw (see text). b) represents all three types of vertices for the φ^6 term. In general, a vertex for the φ^n term is obtained by drawing a point with lines radiating from it. See text for a full discussion.

but instead give the Feynman rules that govern the perturbation expansions in our theory. On expanding out $E[\phi(\boldsymbol{k})]$, we need three types of diagrams (or vertices) to represent each φ^n term in this expansion, for $n > 2$. For illustration some of the diagrams are shown in Figure 14.

Then, we may write down graphs to describe each term in our expansion. Each graph will contain $N_{\rm V}$ vertices, which are all connected to each other by lines. We assign a label $i = 1 \ldots N_{\rm V}$ to each vertex. For each vertex i, representing φ^n, we must write down $\left(a_1(-1)^{n-1} + a_2(-4)^n\right)\delta_{-k_1^i,k_n^i+k_{n-1}^i+\ldots k_2^i}/(2n)!$ and either one of the "form" factors

$$\prod_{m=1}^{2n}\left(1-e^{-ik_{mu}^i r_0}\right), \qquad \prod_{m=1}^{2n}\left(1-e^{-ik_{mv}^i r_0}\right), \qquad \prod_{m=1}^{2n}\left(1-e^{-i(k_{mu}^i-k_{mv}^i)r_0}\right), \quad \text{(A.12)}$$

depending on whether the vertex is type 1, 2 or 3, respectively. Each full Feynman graph will also consist of $N_{\rm E}$ external lines (connected to only one vertex) each associated with a wave vector $\boldsymbol{q}_j$, $(j = 1, \ldots, N_{\rm E})$. For each of these external lines we write down $G(\boldsymbol{q}_j)$ and set $\boldsymbol{k}_m^i = \boldsymbol{q}_j$ for one of the $\boldsymbol{k}_m^i$ in the vertex to which the line is connected. There will also be $N_{\rm I}$ internal lines, each associated with a wave vector $\boldsymbol{p}_k$, $(k = 1, \ldots, N_{\rm I})$, where each end is connected to two vertices, i and i'. For each of these internal lines we write down $G(\boldsymbol{p}_k)$ and set $\boldsymbol{k}_m^i = \boldsymbol{k}_m^{i'} = \boldsymbol{p}_j$ for one of the $\boldsymbol{k}_m^i$ in each of the two vertices. Then all the wave vectors for the internal lines are summed over. Last of all, there is also a symmetry factor that multiplies this, which accounts for how many ways a term (graph) in the expansion may be generated.

To obtain the Hartree approximation we first consider only the graphs for the full correlation function shown in Figure 15. The sum of these graphs we denote by G_1. These form a series which we may easily sum

$$k_{\rm B}TG_1^{-1}(\boldsymbol{k}) = M_1(2-\cos k_u r_0) + M_2(2-\cos k_v r_0) + M_3(2-\cos(k_u-k_v)r_0), \quad \text{(A.13)}$$

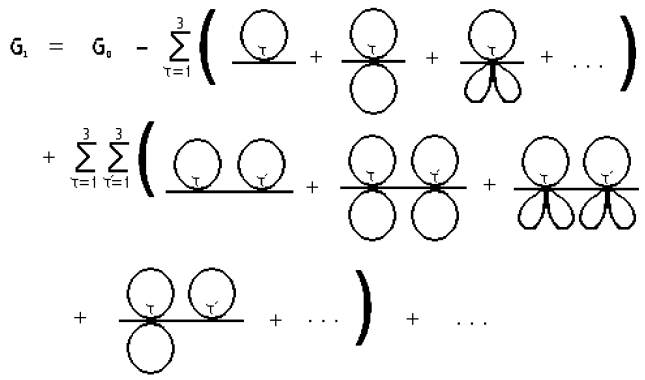

Fig. 15. Graphs that are considered for the full correlation function in the first stage of the Hartree approximation.

Fig. 16. Diagrammatic expansion for the free energy. Here, F_0 is the free energy calculated in the Gaussian approximation.

where

$$M_\tau = -a_1 L \sum_{n=0} \frac{1}{n!} \left(\frac{k_{\rm B}Tc_\tau}{2m_0}\right)^n + 4a_2 L \sum_{n=0} \frac{1}{n!} \left(\frac{2k_{\rm B}Tc_\tau}{m_0}\right). \tag{A.14}$$

The zero-th-order term in the series corresponds to G_0. The first-order term corresponds to the φ^4 vertex, the second-order term to the φ^6 vertex and so on. For c_τ we find the following expression:

$$c_\tau = \frac{1}{Nk_{\rm B}T} \sum_{\boldsymbol{p}} G(\boldsymbol{p}) \left[(2-2\cos(k_u r_0))\delta_{\tau,1} + (2-2\cos(k_v r_0))\delta_{\tau,2} + (2-2\cos((k_u-k_v)r_0))\delta_{\tau,3}\right]. \tag{A.15}$$

From this we may show that $c_\tau = 1/3$ and $M_1 = M_2 = M_3 = m_1$. The next step is to go back to Figure 15 and replace G_0 in each loop with G_1, where G_1 will be replaced on the l.h.s. of this expression with a new correlation function G_2. On summing these graphs we find equation (A.13) (G_1 replaced by G_2), but with $M_1 = M_2 = M_3 = m_1$ where

$$m_2 = -a_1 \exp\left(-\frac{k_{\rm B}T}{6m_1}\right) + 4a_2 \exp\left(-\frac{2k_{\rm B}T}{3m_1}\right). \tag{A.16}$$

We then keep iterating this process until we have $J = m_\infty = m_{\infty-1}$ and so obtain equation (6) of the text.

To calculate the free energy we must consider the sum of graphs (Fig. 16). For the free energy in the Hartree approximation we take care in replacing m_0 with J, renormalizing our expansion, thus obtaining equation (5) of the text.

Appendix B. The Hartree approximation for the quasi-antiferromagnetic state

In the QAF state we now have spontaneous symmetry breaking where

$$\langle \phi_{j,l} - \phi_{j-1,l} \rangle = \langle \phi_{j,l} - \phi_{j-1,l+1} \rangle = \psi \neq 0 \quad \text{and} \quad \langle \phi_{j,l} - \phi_{j,l-1} \rangle = 0. \tag{B.1}$$

To take account of equation (B.1) we rewrite $\phi_{j,l} - \phi_{j-1,l} = \psi + \phi'_{j,l} - \phi'_{j-1,l}$, $\phi_{j,l} - \phi_{j-1,l+1} = \psi + \phi'_{j,l} - \phi'_{j-1,l+1}$ and $\phi_{j,l} - \phi_{j,l-1} = \phi'_{j,l} - \phi'_{j,l-1}$. We then rewrite equation (A.2) in the following form:

$$E[\phi_{jl}] = L \sum_{p=1}^{2} \sum_{jl} a_p (-1)^p \left[[\cos(p(\phi'_{j,k} - \phi'_{j,l-1})) - \cos(p\psi)(\cos(p(\phi'_{j,l} - \phi'_{j-1,l})) + \cos(p(\phi_{j,l} - \phi_{j-1,l+1})))] - [\sin(p\psi)(\sin(p(\phi'_{j,l} - \phi'_{j-1,l})) + \sin(p(\phi'_{j,l} - \phi'_{j-1,l+1})))] \right]. \tag{B.2}$$

Expanding in powers of we may again divide the energy into Gaussian and anharmonic terms:

$$E[\phi_{j,l}] = E_0[\phi_{j,l}] + E^{(1)}_{\rm anh}[\phi_{j,l}] + E^{(2)}_{\rm anh}[\phi_{j,l}],$$

$$E_0[\phi_{j,l}] = NL(a_2 - a_1) + 2NL(a_2\cos(2\psi) - a_1\cos(\psi)) + L(a_1\sin(\psi) - 2a_2\sin(2\psi))\Delta\phi'_{\rm boundary} + \frac{1}{2}\sum_{jl} \left[\tilde{m}_{0,1}(\phi'_{j,l} - \phi'_{j-1,l})^2 + \tilde{m}_{0,2}(\phi'_{j,l} - \phi'_{j,l-1})^2 + \tilde{m}_{0,1}(\phi'_{j,l} - \phi'_{j-1,l+1})^2\right], \tag{B.3}$$

$$E^{(1)}_{\rm anh}[\phi_{j,l}] = L \sum_{jl} \sum_{n=2}^{\infty} \frac{1}{(2n)!} \left\{ \left(a_1(-1)^{n-1} + a_2(-4)^n\right) \times \left(\phi'_{j,l} - \phi'_{j,l-1}\right)^{2n} + \left(a_1(-1)^{n-1}\cos(\psi) + \cos(2\psi)a_2(-4)^n\right) \times \left(\left((\phi'_{j,l} - \phi'_{j-1,l})^{2n} + (\phi'_{j,l} - \phi'_{j-1,l+1})^{2n}\right)\right) \right\},$$

$$E^{(2)}_{\rm anh}[\phi_{j,l}] = L \sum_{jl} \sum_{n=2}^{\infty} \frac{1}{(2n-1)!} \left[\left(a_1 \sin\psi(-1)^{n-1} + a_2\sin(2\psi)(-4)^n/2\right) \left((\phi'_{j,l} - \phi'_{j-1,l})^{2n-1} + (\phi'_{j,l} - \phi'_{j-1,l+1})^{2n-1}\right)\right],$$

where

$$\Delta\phi'_{\rm boundary} = \sum_{jl} \left((\phi'_{j,l} - \phi'_{j-1,l}) + (\phi'_{j,l} - \phi'_{j-1,l+1})\right), \tag{B.4}$$

$\tilde{m}_{0,1} = L(a_1\cos\psi - 4a_2\cos 2\psi)$ and $\tilde{m}_{0,2} = L(a_1 - 4a_2)$. Again, let us consider Gaussian fluctuations and so discard all anharmonic terms. $\Delta\phi'_{\rm boundary}$ is the difference in ϕ' (fluctuations in ϕ) between one part of the boundary and

another part of the boundary of our lattice, which cannot be neglected. We can think of the coefficient that multiplies $\Delta\phi'_{\text{boundary}}$ as a net torque, which is non-zero when the system is out of equilibrium. At equilibrium, therefore, we require that, for the $\Delta\phi'_{\text{boundary}}$ term to vanish,

$$\cos\psi = \frac{a_1}{4a_2} \text{ or } \sin\psi = 0. \tag{B.5}$$

Indeed, through our definition of ψ; $\left\langle \phi'_{j,l} - \phi'_{j-1,l+1} \right\rangle$, $\left\langle \phi'_{j,l} - \phi'_{j,l-1} \right\rangle$ and $\left\langle \phi'_{j,l} - \phi'_{j-1,l} \right\rangle$ must vanish, which occurs only if equation (B.5) is satisfied. If only the first condition of equation (B.5) is satisfied, only fluctuations around the antiferromagnetic state are under consideration. The second condition corresponds to fluctuations in the ferromagnetic state (cf. App. A).

Now, we are able to perform the integrations over ϕ and so arrive at the free energy

$$\begin{aligned} F_0 &= NL(a_1 - a_2) + 2NL(a_1\cos(\psi) - a_2\cos(2\psi)) \\ &+ \frac{k_{\text{B}}TNL}{2(2\pi)^2}\int_{-\pi}^{\pi}\mathrm{d}x\int_{-\pi}^{\pi}\mathrm{d}y \ln\left(\frac{1}{\pi}\left[\tilde{m}_{0,1}(2-\cos x)\right.\right. \\ &\left.\left.+\tilde{m}_{0,2}(2-\cos y) + \tilde{m}_{0,1}(2-2\cos(x-y))\right]\right). \end{aligned} \tag{B.6}$$

We shall leave the evaluation of this integral until later.

To obtain the Hartree approximation we proceed in the same manner as in Appendix A and sum the same graphs for both the free energy and the correlation function. Summing up all the graphs in Figure 15 we find that equations (A.13) and (A.14) still hold with $\tilde{m}_{0,1}$ replacing m_0, but now

$$\begin{aligned} c_\tau &= \frac{1}{N}\sum_{\boldsymbol{p}} G(\boldsymbol{p})[(2-2\cos(k_u r_0))\delta_{\tau,1} \\ &+ (2-2\cos(k_v r_0))\delta_{\tau,2} + (2-2\cos((k_u-k_v)r_0))\delta_{\tau,3}] = \\ &\frac{1}{(2\pi)^2}\int_{-\pi}^{\pi}\mathrm{d}x\int_{-\pi}^{\pi}\mathrm{d}y \\ &\times\frac{[(2-2\cos(x))\delta_{\tau,1}+(2-2\cos(y))\delta_{\tau,2}+(2-2\cos(x-y))\delta_{\tau,3}]}{(2-2\cos(x))+\beta_0(2-2\cos(y))+(2-2\cos(x-y))}, \end{aligned} \tag{B.7}$$

where $\beta_i = \tilde{m}_{i,2}/\tilde{m}_{i,1}$ and $c_1 = c_3 \neq c_2$.

There is an important completeness relation $2c_1 + \beta c_2 \equiv 1$. We may evaluate one of the integrals and determine the other through this relation. We find

$$\begin{aligned} c_1(\beta) &= \frac{2}{\pi}\arcsin\left(\frac{1}{\sqrt{2(\beta+1)}}\right), \\ c_2(\beta) &= \frac{1}{\beta}\left(1 - \frac{4}{\pi}\arcsin\frac{1}{\sqrt{2(\beta+1)}}\right). \end{aligned} \tag{B.8}$$

So now we are able to set $M_1 = M_3 = \tilde{m}_{1,1}$ and $M_2 = \tilde{m}_{1,2}$ in equation (A.13). Again, we go back to Figure 15 and replace G_0 in each loop with G_1, and replace G_1 on the l.h.s. with a new correlation function G_2. So we have equation (A.13), but with $M_1 = M_3 = \tilde{m}_{2,1}$ and $M_2 = \tilde{m}_{2,2}$, where

$$m_{2,\tau} = -a_1\exp\left(-\frac{kTc_\tau(\beta_1)}{2\tilde{m}_{1,0}}\right) + 4a_2\exp\left(-\frac{2kTc_\tau(\beta_1)}{\tilde{m}_{1,0}}\right). \tag{B.9}$$

We again keep iterating this process until we have $J_1 = m_{\infty,1} = m_{\infty-1,1}$ and $J_2 = m_{\infty,2} = m_{\infty-1,2}$. Consequently, we obtain

$$\begin{aligned} J_1 &= L\left\{a_1\cos\psi\exp\left(-\tfrac{k_{\text{B}}T}{2J_1}c_1(\alpha)\right) - 4a_2\cos 2\psi\exp\left(-\tfrac{2k_{\text{B}}T}{J_1}c_1(\alpha)\right)\right\} \\ J_2 &= L\left\{a_1\exp\left(-\tfrac{k_{\text{B}}T}{2J_1}c_2(\alpha)\right) - 4a_2\exp\left(-\tfrac{2k_{\text{B}}T}{J_1}c_2(\alpha)\right)\right\}, \end{aligned} \tag{B.10}$$

where $\alpha = J_2/J_1$. To obtain the free energy, again, we must consider the sum of graphs shown in Figure 16. To get the free energy in the Hartree approximation we replace $\tilde{m}_{0,1}$ with J_1 and $\tilde{m}_{0,2}$ with J_2. Renormalizing the free energy we find

$$\begin{aligned} F_{\text{af}} &= \frac{Nk_{\text{B}}T}{2}\ln\left(\frac{J_1}{k_{\text{B}}T}\right) + \frac{Nk_{\text{B}}T}{6}\tilde{\Omega}_{\text{af}}\left(\alpha+\frac{1}{2}\right) + Nk_{\text{B}}T\hat{C}_{\text{Hex}} \\ &+ 2NL\left[a_0 - a_1\cos(\psi)\exp\left(-\frac{k_{\text{B}}T}{2J_1}c_1(\alpha)\right)\right. \\ &\left.+a_2\cos(2\psi)\exp\left(-\frac{2k_{\text{B}}T}{J_1}c_1(\alpha)\right)\right] \\ &+ NL\left[a_0 - a_1\exp\left(-\frac{k_{\text{B}}T}{2J_2}c_2(\alpha)\right)\right. \\ &\left.+a_2\exp\left(-\frac{2k_{\text{B}}T}{J_2}c_2(\alpha)\right)\right], \end{aligned} \tag{B.11}$$

where $\tilde{\Omega}_{\text{af}}(\alpha+\frac{1}{2})$ is determined through the following relationship:

$$\begin{aligned} \tilde{\Omega}_{\text{af}}\left(\alpha+\frac{1}{2}\right) &= \frac{1}{(2\pi)^2}\int_{-\pi}^{\pi}\mathrm{d}x\int_{-\pi}^{\pi}\mathrm{d}y \\ &\times\ln\left(\frac{[(2-\cos x)+\alpha(2-\cos y)+(2-2\cos(x-y)]}{[(2-\cos x)+(2-\cos y)+(2-2\cos(x-y)]}\right) = \\ &\int_1^\alpha \mathrm{d}\alpha'\frac{1}{\alpha'}\left(1 - \frac{4}{\pi}\arcsin\frac{1}{\sqrt{2(\alpha'+1)}}\right). \end{aligned} \tag{B.12}$$

We could not find a closed form for this integral. Therefore, we have approximated it with a logarithm and Padé approximants that interpolate between the Taylor expansion of $\tilde{\Omega}_{\text{af}}(x)$ in powers of $x^{1/2}$ around $\tilde{\Omega}_{\text{af}}(0)$ and an asymptotic expansion.

Now, all the terms in $E^{(2)}_{\text{anh}}[\phi_{j,l}]$ will contribute with the requirement (from equation (B.1)) that

$$\begin{aligned} \left\langle \phi'_{j,l} - \phi'_{j-1,l} \right\rangle &= \lim_{p\to 0}(1-\exp(-iq_u r_0)\Gamma(\boldsymbol{q},\psi)) = 0, \\ \left\langle \phi'_{j,l} - \phi'_{j-1,l+1} \right\rangle &= \lim_{p\to 0}(1-\exp(-i(q_u-q_v)r_0)\Gamma(\boldsymbol{q},\psi)) = 0. \end{aligned} \tag{B.13}$$

Equation (B.13) will constrain the value of ψ as in the Gaussian approximation. We find the following expression

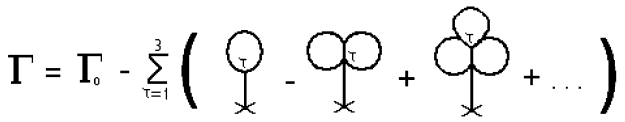

Fig. 17. Diagrammatic expansion for $\Gamma(\boldsymbol{p},\psi)$. Here, $\Gamma_0 = a_1\sin(\psi) - 2a_2\sin(2\psi)$, and in the Gaussian approximation, $\Gamma(\boldsymbol{p},\psi) = \Gamma_0$. Usual Feynman rules apply, except there is one additional rule: the external line ending in a cross has no G_0 associated with it.

for $\Gamma(\boldsymbol{q},\psi)$:

$$\Gamma(\boldsymbol{q},\psi) \equiv \sum_{n=0}^{\infty} \frac{a_1\sin(\psi)\,(-c_1 k_{\rm B}T/(2\tilde{m}_{0,1}))^n - 2a_2\sin(2\psi)\,(-2c_1 k_{\rm B}T/\tilde{m}_{0,1})^n}{n!} = a_1\sin(\psi)\exp\left(-\frac{k_{\rm B}Tc_1}{2\tilde{m}_{0,1}}\right) - a_2\sin(2\psi)\exp\left(-\frac{2k_{\rm B}Tc_1}{\tilde{m}_{0,1}}\right). \quad \text{(B.14)}$$

Each term in this series can be represented diagrammatically as in Figure 17. To get the Hartree approximation, equation (B.14) should be renormalized by replacing $\tilde{m}_{0,1}$ with J_1 and β with α, and so replacing G_0 by G_∞ in each of the loops. For equation (B.13) to be satisfied we require that $\Gamma(\boldsymbol{p},\psi) = 0$. This gives us the following equations for ψ:

$$\cos(\psi) = \frac{a_1}{4a_2}\exp\left(\frac{3k_{\rm B}Tc_1(\alpha)}{2J_1}\right) \text{ or } \sin(\psi) = 0. \quad \text{(B.15)}$$

The set of equations (B.15), (B.10) and (B.11) form a complete set for the QAF state.

For the QAF state on a hexagonal lattice close to $T = 0$, from equation (B.5) it follows that $\beta \le -1/2$. The upshot of this is that $c_1(\beta)$ and $c_2(\beta)$ are complex unless $\beta = -1/2$ (at $a_1/4a_2 = 1$), and the QAF state at $T = 0$ is unstable. Therefore, it cannot be a ground state except at the point of frustration. At $T \neq 0$ we find that thermal fluctuations can stabilize the QAF state. However, this state always has a higher free energy than either the Potts or ferromagnetic states, so will not be a phase of the system at thermal equilibrium.

If we allow the lattice to distort to the rhombic structure described in the text, we have

$$E[\phi_{j,l}] = L\sum_{p=1}^{2}\sum_{jl}(-1)^p[a_p(R_2)\cos(p(\phi_{j,k}-\phi_{j,l-1})) + a_p(R_1)\cos(p(\phi_{j,l}-\phi_{j-1,l})) + a_p(R_1)\cos(p(\phi_{j,l}-\phi_{j-1,l+1}))]. \quad \text{(B.16)}$$

On inspection of equation (B.16), it is easy to modify equations (B.10), (B.11) and (B.15) so as to arrive at equations (11) and (12) of the text.

Appendix C. The Hartree approximation for the Potts state

This is perhaps the most difficult of the states we must consider, as so many of the lattice symmetries are broken.

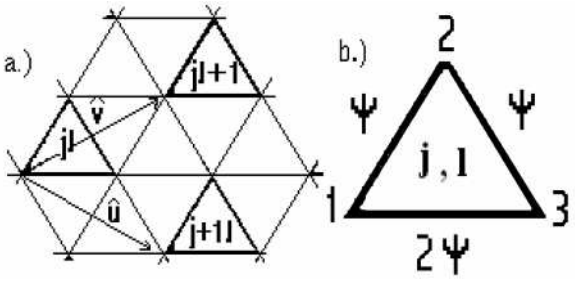

Fig. 18. a) Lattice construction for the Potts state where and now correspond to new lattice vectors for this new unit cell. Here, we have constructed a new unit cell with the basis shown in b). Each of the three sites in the basis is given a label (1, 2 or 3). This is to take into account the broken lattice symmetries of the Potts state. Also shown is the magnitude of the difference in $\langle\phi\rangle$ between each neighboring site, which may either be ψ or 2ψ.

To perform calculations we must make the construction shown in Figure 18. Then, essentially, we must rewrite equation (A.2)

$$E = E_1 + E_2 + E_3,$$

$$E_1 = \frac{1}{2}\sum_{p=1}^{2}\sum_{j,l} a_p(-1)^p \times [\cos(p(\phi_{1,j,l}-\phi_{2,j,l})) + \cos(p(\phi_{1,j,l}-\phi_{2,j,l-1})) + \cos(p(\phi_{1,j,l}-\phi_{2,j+1,l-1})) + \cos(p(\phi_{1,j,l}-\phi_{3,j,l})) + \cos(p(\phi_{1,j,l}-\phi_{3,j,l-1})) + \cos(p(\phi_{1,j,l}-\phi_{3,j-1,l}))],$$

$$E_2 = \frac{1}{2}\sum_{p=1}^{2}\sum_{j,l} a_p(-1)^p \times [\cos(p(\phi_{2,j,l}-\phi_{3,j,l})) + \cos(p(\phi_{2,j,l}-\phi_{3,j-1,l+1})) + \cos(p(\phi_{2,j,l}-\phi_{3,j-1,l})) + \cos(p(\phi_{2,j,l}-\phi_{1,j,l})) + \cos(p(\phi_{2,j,l}-\phi_{1,j-1,l+1})) + \cos(p(\phi_{2,j,l}-\phi_{1,j,l+1}))],$$

$$E_3 = \frac{1}{2}\sum_{p=1}^{2}\sum_{j,l} a_p(-1)^p \times [\cos(p(\phi_{3,j,l}-\phi_{1,j,l})) + \cos(p(\phi_{3,j,l}-\phi_{1,j,l+1})) + \cos(p(\phi_{3,j,l}-\phi_{1,j+1,l})) + \cos(p(\phi_{3,j,l}-\phi_{2,j,l})) + \cos(p(\phi_{3,j,l}-\phi_{2,j+1,l})) + \cos(p(\phi_{3,j,l}-\phi_{2,j+1,l-1}))], \quad \text{(C.1)}$$

where we have introduced the angles ϕ_n, where $n = 1, 2, 3$, according to their location on the lattice (the sites are defined in Fig. 18). Then, we must expand out this expression around the Potts state, which we may do by writing $\phi_{1,j,l} = \hat{\phi}_{1,j,l}$, $\phi_{2,j,l} = \psi + \hat{\phi}_{2,j,l}$ and $\phi_{3,j,l} = 2\psi + \hat{\phi}_{3,j,l}$. The expressions we get are cumbersome and we shall not write them down. For brevity's sake, in what follows we shall only give an outline of the derivation and only state key results.

$$G_0^{-1}(\boldsymbol{k}) = \frac{\tilde{m}_{0,1}}{k_{\rm B}T}\begin{pmatrix} 3(1+\beta_0) & -1-e^{-ik_v r_0}+e^{-i(k_v-k_u)r_0} & -\beta_0(1+e^{-ik_v r_0}+e^{-ik_u r_0}) \\ -1-e^{ik_v r_0}-e^{i(k_v-k_u)r_0} & 6 & -1-e^{ik_u r_0}-e^{i(k_u-k_v)r_0} \\ -\beta_0(1+e^{ik_v r_0}+e^{ik_u r_0}) & -1-e^{ik_u r_0}-e^{i(k_u-k_v)r_0} & 3(1+\beta_0) \end{pmatrix}, \tag{C.3}$$

The next step is to separate E into a Gaussian (E_0) and anharmonic part ($E_{\rm anh}$) in the same way as we did for the other states. We may Fourier transform these to reciprocal space using relations similar to equation (A.4). Here we state a key result, that

$$E_0 = \frac{1}{2}\sum_{\boldsymbol{k}} \boldsymbol{\phi}^T(-\boldsymbol{k})G_0^{-1}(\boldsymbol{k})\boldsymbol{\phi}(\boldsymbol{k}) \tag{C.2}$$

where $G_0^{-1}(\boldsymbol{k})$ is given by

see equation (C.3) *above*

$\boldsymbol{\phi} = (\phi_1, \phi_2, \phi_3)$ and $\beta_i = \tilde{m}_{i,2}/\tilde{m}_{i,1}$. We now define $\tilde{m}_{0,1} = a_1\cos(\psi) - 4a_2\cos(2\psi)$ and $\tilde{m}_{0,2} = a_1\cos(2\psi) - 4a_2\cos(4\psi)$. To obtain the Hartree result for the correlation function we consider the same graphs as in Figure 15. Now, however, each G_0 is a 3×3 matrix, the inverse matrix of G_0^{-1} given in equation (C.3). On summation of these graphs we find equation (C.3), but with G_0^{-1}, β_0 and $\tilde{m}_{0,1}$ replaced by G_1^{-1}, β_1 and $\tilde{m}_{1,1}$, respectively, where $\tilde{m}_{1,1}$ and $\tilde{m}_{1,2}$ are determined through the following relations:

$$\tilde{m}_{1,s} = -a_1\exp\left(-\frac{k_{\rm B}T\eta_s(\beta_0)}{\tilde{m}_{0,1}}\right) + 4a_2\exp\left(-\frac{4k_{\rm B}T\eta_s(\beta_0)}{\tilde{m}_{0,1}}\right), \tag{C.4}$$

where $s = 1$ or 2,

$$\begin{aligned}\eta_1(\beta) &= \frac{1}{2(2\pi)^2}\int_{-\pi}^{\pi}{\rm d}x\int_{-\pi}^{\pi}{\rm d}y\,\big[(10+26\beta+6\beta^2) \\ &-(5+7\beta+2\beta^2)(\cos x+\cos(y))-(8+10\beta+2\beta^2)\cos(x-y) \\ &-\beta(\cos(x-2y)+\cos(2x-y))\big]\,G(x,y)^{-1}, \\ \eta_2(\beta) &= \frac{1}{(2\pi)^2}\int_{-\pi}^{\pi}{\rm d}x\int_{-\pi}^{\pi}{\rm d}y\,[13+12\beta-(4+6\beta)(\cos x+\cos y) \\ &-5\cos x\cos y-3\sin y\sin x]\,G(x,y)^{-1}\end{aligned} \tag{C.5}$$

and

$$\begin{aligned}G(x,y;\beta) = {}& 6(6+13\beta+6\beta^2) \\ &-12(1+\beta)^2(\cos x+\cos y+\cos(x+y)) \\ &-2\beta(\cos(x+y)+\cos(2x-y)+\cos(x-2y)).\end{aligned} \tag{C.6}$$

We may then calculate G_2^{-1} as we did in the previous expressions. We find again equations (C.3) and (C.4), but with G_1^{-1}, $\tilde{m}_{0,1}$, $\tilde{m}_{0,2}$, $\tilde{m}_{1,1}$ and $\tilde{m}_{1,2}$ all replaced by G_2^{-1}, $\tilde{m}_{1,1}$, $\tilde{m}_{1,2}$, $\tilde{m}_{2,1}$ and $\tilde{m}_{2,2}$, respectively. On further iteration (as described in previous appendices), we obtain equations (8a) and (8b). Again we have used Padé approximants for $\eta_1(\beta)$ and $\eta_2(\beta)$.

In order to obtain the free energy again, we must consider the sum of graphs shown in Figure 16, but with each G_0 a matrix. Then, we replace $\tilde{m}_{0,1}$ with J_1 and $\tilde{m}_{0,2}$ with J_2, obtaining equation (8) with

$$\tilde{\Omega}_{\rm potts}(\alpha) = \frac{1}{(2\pi)^2}\int_{-\pi}^{\pi}{\rm d}x\int_{-\pi}^{\pi}{\rm d}y\ln\left(\frac{G(x,y;\alpha)}{G(x,y;1)}\right). \tag{C.7}$$

$\Gamma(\boldsymbol{k},\psi)$ is now a matrix, and is determined by first considering the graphs shown in Figure 17 (where G_0 is also a matrix) and then replacing $\tilde{m}_{0,1}$ with J_1 and β with α. This enables us to derive equation (8c) of the text.

References

1. F. Livolant, A. Leforestier, Prog. Polym. Sci. **21**, 1115 (1996).
2. R. Langridge, H.R. Wilson, C.W. Hooper, M.H.F. Wilkins, L.D. Hamilton, J. Mol. Biol. **2**, 19 (1960).
3. C. Robinson, Tetrahedron **13**, 219 (1961).
4. H.H. Strey *et al.*, Phys. Rev. Lett. **84**, 3105 (2000).
5. T.E. Strzelecka, M.W. Davidson, R.L. Rill, Nature **331**, 457 (1988).
6. Z. Reich, E.J. Wachtel, A. Minsky, Science **264**, 1460 (1994).
7. V.A. Bloomfield, Curr. Opin. Struct. Biol. **6**, 334 (1996).
8. W.M. Gelbart, R.F. Bruinsma, P.A. Pincus, V.A. Parsegian, Phys. Today **53**, 38 (2000).
9. H.H. Strey, R. Podgornik, D.C. Rau, V.A. Parsegian, Curr. Opin. Struct. Biol. **8**, 309 (1998).
10. R. Podgornik, H.H. Strey, V.A. Parsegian, Curr. Opin. Colloid Interface Sci. **3**, 534 (1998).
11. B.M. Weiner, N. Kleckner, Cell **77**, 977 (1994).
12. F. Oosawa, Biopolymers **6**, 134 (1968).
13. A.A. Kornyshev, S. Leikin, J. Chem. Phys. **107**, 3656 (1997); **108**, 7035(E) (1998).
14. A.A. Kornyshev, S. Leikin, Phys. Rev. Lett. **82**, 4138 (1999).
15. A.A. Kornyshev, S. Leikin, Biophys. J. **75**, 2513 (1998).
16. H.M. Harreis, A.A. Kornyshev, C.N. Likos, H. Löwen, G. Sutmann, Phys. Rev. Lett. **89**, 018303 (2002).
17. V. Lorman, R. Podgornik, B. Žekš, Phys. Rev. Lett. **87**, 218101 (2001).
18. A.A. Kornyshev, S. Leikin, Phys. Rev. E **62**, 2576 (2000).
19. A.A. Kornyshev, S. Leikin, Phys. Rev. Lett. **86**, 3666 (2001) (*DNA need not unzip*, Phys. Rev. Focus (`http://focus.aps.org/v7/st19.html`)).
20. D.J. Lee, A. Wynveen, A.A. Kornyshev, Phys. Rev. E **70**, 051913 (2004).
21. R.B. Potts, Proc. Cambridge Philos. Soc. **48**, 106 (1952).
22. A.G. Cherstvy, A.A. Kornyshev, S. Leikin, J. Phys. Chem. B **108**, 6508 (2004).

23. S. Samuel, Phys. Rev. B **25**, 1755 (1982).
24. J.M. Kosterlitz, D.J. Thouless, J. Phys. C **6**, 1181 (1973).
25. There are 6 distinct topological ground states corresponding to the broken symmetries of the Potts state. 3 states are got through translations of the lattice, the other three are got by changing the staggered helicity (defined later in the text). However, what seems to matter in this transition is the change in staggered helicity.
26. D.H. Lee, J.D. Joannopoulos, J.W. Negele, D.P. Landau, Phys. Rev. B **33**, 450 (1986).
27. Unfortunately, including topological excitations in a systematic manner is an involved and difficult process. Indeed, in the pure XY model vortices have been included in analytical calculations (S. Ami, H. Kleinert, Phys. Rev. B **33**, 4692 (1986)). These calculations are complicated, but do lead to a good agreement from zero temperature right up to the BKT transition. However, we have decided that, since this is a first time study, a theoretical treatment including topological excitations is beyond the scope of the present work.
28. A.G. Cherstvy, A.A. Kornyshev, S. Leikin, J. Phys. Chem. B **106**, 13362 (2002).
29. T.E. Strzelecka, R.L. Rill, J. Am. Chem. Soc. **109**, 4513 (1987).
30. D. Durand, J. Doucet, F. Livolant, J. Phys. II **2**, 1769 (1992).
31. E. Allahyarov, G. Gompper, H. Löwen, Phys. Rev. E **69**, 041904 (2004).
32. A.H.A. Tajmir-Riahi *et al.*, J. Biomol. Struct. Dyn. **11**, 83, (1993); I. Fita *et al.*, J. Mol. Biol. **167**, 157 (1983); N.V. Hud *et al.*, Biochemistry **33**, 7528 (1994); X. Shui *et al.*, Biochemistry **37**, 8341 (1998).
33. A.A. Kornyshev, D.J. Lee, S. Leikin, A. Wynveen, S.B. Zimmerman, in preparation.
34. K. Kassapidou, J.R.C. van der Maarel, Eur. Phys. J. B **3**, 471 (1998).
35. For a review see, A.A. Kornyshev, in *The Chemical Physics of Solvation, Part A: Theory of Solvation*, edited by R.R. Dogonadze, E. Kalman, A.A. Kornyshev, J. Ulstrup (Elsevier, Amsterdam, 1985) Chapt. 3; M.A. Vorotyntsev, A.A. Kornyshev, *Electrostatic of Media with the Spatial Dispersion* (Nauka, Moscow, 1993); A.A. Kornyshev, G. Sutmann, *Static and Dynamic Nonlocal Dielecric Response of Water*, in *Electron and Ion Transfer in Condensed Media* edited by A.A. Kornyshev, M.P. Tosi, J. Ulstrup (World Scientific, Singapore, 1997).
36. A.A. Kornyshev, A. Wynveen, Phys. Rev. E **69**, 041905 (2004).
37. As an example using the hexagonal Brillouin zone, see C. Honerkamp, Phys. Rev. B **68**, 104510 (2003).
38. For those interested in the steps in the calculation but less experienced in diagrammatic perturbation theory, we refer to Daniel J. Amit, *Field Theory, the Renormalization Group, and Critical Phenomena* (World Scientific, 1997); Jean Zinn-Justin, *Quantum Field Theory and Critical Phenomena* (Oxford Science Publications, 2001).